OPTICA

Spatiotemporal electric-field characterization of synthesized light transients

Mikhail Mamaikin,[1,*] Enrico Ridente,[1,2] Ferenc Krausz,[1,3] and Nicholas Karpowicz[1,3,4]

[1]Max-Planck-Institut für Quantenoptik, Hans-Kopfermann-Strasse 1, 85748 Garching, Germany
[2]Currently at Department of Chemistry, University of California, Berkeley, Berkeley, California 94720, USA
[3]Fakultät für Physik, Ludwig-Maximilians-Universität, Am Coulombwall 1, 85748 Garching, Germany
[4]nicholas.karpowicz@mpq.mpg.de
*mikhail.mamaikin@mpq.mpg.de

Received 2 October 2023; revised 28 November 2023; accepted 5 December 2023; published 12 January 2024

The versatile manipulation of electron motion on the atomic scale calls for the shaping of the electric field evolution of light within a single cycle. The super-octave bandwidth required for this task dramatically increases the probability of formation of spatio-temporal distortions. As a result, the accuracy of physical observables can be extremely compromised by spatial averaging unless the complete spatio-temporal field information is known. Here, we apply spatially resolved electro-optic sampling to record three-dimensional electric-field structure of a sub-cycle synthesized light transient carrying wavelengths from 700 to 2700 nm. We show an in-depth picture of the field synthesis process, disclosing how temporal, spectral, and global-phase properties of the synthesized pulse vary across space, including the propagation direction around the focal point where the transient is generated.

https://doi.org/10.1364/OPTICA.507219

1. INTRODUCTION

The generation of few-cycle laser pulses has opened new avenues into the study of fundamental properties of light–matter interaction [1–6]. Few-cycle pulses in the visible and near-infrared spectral regions have facilitated, for example, the observation of ultrafast changes in the optical properties of solids [7] and the sub-femtosecond energy transfer from light to electrons [8]. The transition into the single- and sub-cycle regimes becomes essential for the precise control and manipulation of atomic-scale electron motion in solids and molecules. To break the single-cycle limit, pulses containing multi-octave bandwidths must be produced. The difficulty of temporal compression and waveform control over such spectral bandwidth arises for frequencies approaching the petahertz scale. Lately, this has been bypassed using the concept of pulse synthesis, where a single-to-sub-cycle light transient can be shaped by coherently combining multiple spectral channels from separate laser sources [9,10], optical parametric amplifiers [11–14], or subdivided spectral bands after the fiber broadening [15–17].

The measurement of light transients is a challenging task, as the envelope approximation is no longer applicable. The carrier envelope phase (CEP), also called the global phase in the context of light transients [16], has a strong impact on the shape of the electric field. This leads to different matter responses in strong-field experiments triggered by pulses with different global phases [18,19]. Therefore, the question of the complete characterization of such pulses is linked to recording the electric field itself. The strong temporal confinement required to measure field oscillations in the near-infrared and visible has been first realized through high harmonic generation and complex vacuum beamlines [20,21]. More recent advances in field sampling technologies, such as tunneling ionization with a perturbation for the time-domain observation of an electric field (TIPTOE) [22–24], photoconductive sampling [25–27], and electro-optic sampling (EOS) [17,28,29] and its generalized counterparts [30], allow attosecond experiments to be easily conducted under ambient conditions.

Typically, physical observables in laser experiments result from the spatial averaging of the interaction volume within the incident beam cross section. In the case of significant spatiotemporal inhomogeneities of the exciting light field, the accuracy of the macroscopic observables used to access the underlying microscopic processes will be highly compromised by the spatial averaging. The ultrabroad bandwidth associated with light transients drastically increases the probability of accidental formation of various spatiotemporal distortions. The reasons behind their emergence are multifold: from simple optical elements [31] and multilayer mirrors [32] to parametric amplification of the channels [33] and their spatial superposition. Therefore, it is crucial to capture not only the space-averaged temporal evolution of the electric field but also the complete spatio-temporal structure of broadband pulses.

Although significant progress has been made in this direction, most of the current techniques record spatio-spectral information of a pulse using interferometry with a reference beam, thus requiring phase-retrieval algorithms and an extra measurement in the time domain to reconstruct the complete field [34–39]. Another way of resolving the electric field in time and space with

high resolution is a raster scan with a metal tip [40,41] or CEP-sensitive nanostructures [42], operating under conditions of long stability and reproducibility of sampled pulses. Unfortunately, interferometric and raster methods lack direct and fast access to the spatiotemporal structure of laser pulses. An alternative approach has been presented by imaging based on EOS, popular in the terahertz community [43–45] and only recently brought to the near-infrared spectral range [46]. EOS imaging yields broadband microscopy of electric fields with sub-wavelength resolution in time and space in a wide-field geometry.

In this paper, we show the synthesis of a sub-cycle light transient centered at 1.7 μm with a 4.5 fs pulse duration and its complete field characterization directly in the spatio-temporal domain. While a solely temporal reconstruction displays an optimal shape of our synthesized electric field for attosecond experiments, we reveal arbitrary spatio-temporal effects that are averaged in standard field sampling techniques. The measurement utilizes spatially resolved EOS, which is applied to image ultra-broadband pulses in the near-infrared and visible spectral range, up to 450 THz. Using this technology, we demonstrate how field properties of the light transient vary across space including numerical field reconstruction along the propagation direction.

2. EXPERIMENTAL SYSTEM AND ELECTRO-OPTIC SAMPLING

The laser system previously reported in [16,47] utilizes 0.7 mJ, 15 fs pulses centered at 1.8 μm, spectrally broadened in a hollow-core fiber under ambient conditions. The output supercontinuum spans over three octaves from the ultraviolet to the infrared spectral range, 300–2700 nm. As shown in Fig. 1, the spectrum is split into three channels using custom-made dichroic beam splitters: ultraviolet-visible (UV-VIS, 300–600 nm), visible-near-infrared (VIS-NIR, 700–1400 nm) and infrared (IR, 1400–2700 nm). The channels are recollimated and individually compressed using a chirped-mirror compressor (CMC) to 2.8 fs, 6.8 fs, and 12.5 fs, respectively.

Light transients can be generated through the coherent recombination of the channels with delay stages. In our experiment, we combine two long-wavelength channels, VIS-NIR and IR, to synthesize a sub-cycle transient at a central wavelength of 1.7 μm (with a period carrier frequency of 5.6 fs). To measure the temporal evolution of the synthesized field, we use the EOS technique and employ the UV-VIS channel as a sampling pulse. As was shown in [16], the bandwidth of this channel supports the detection of frequencies up to 0.5 PHz. The synthesized and sampling pulses after recombination are focused on a 5-μm-thick, type-I beta barium borate (BBO) crystal. The nonlinear process between the pulses is phase-matched for sum-frequency generation (SFG), where the newly generated wave is emitted on the perpendicular axis ($o + o = e$). The EOS signal is produced by the interference of the SFG with an overlapping spectrum within the sampling pulse (local oscillator, LO) on photodiodes after their projection [29]. By varying the time delay between the two pulses, a temporal reconstruction of the synthesized electric field can be recorded. Figure 2(a) shows an EOS measurement of the 4.5-fs synthesized field $E(t)$, the spectrum of which is obtained via Fourier transform and shown in Fig. 2(b). The retrieved time-domain waveform exhibits a high degree of field asymmetry, which is particularly beneficial for studying attosecond and strong-field phenomena.

3. ELECTRIC-FIELD IMAGING OF SYNTHESIZED PULSE

Since EOS is an all-optical approach to measure electric fields, the spatial information of the pulse under study is also carried to the detector but averaged due to the use of photodiodes. Therefore, the spatiotemporal properties of the pulse cannot be probed. A simple imaging system can access the spatial domain in the transverse direction, providing time-varying field oscillations at each pixel. The ratio of the beam sizes in the BBO between the sampling pulse and the synthesized field must be carefully adjusted (~6 times in our case) to fully resolve the field structure and mitigate errors due to the spatiotemporal effects of the sampling pulse. To image the nonlinear interaction between the pulses, we use an approximately

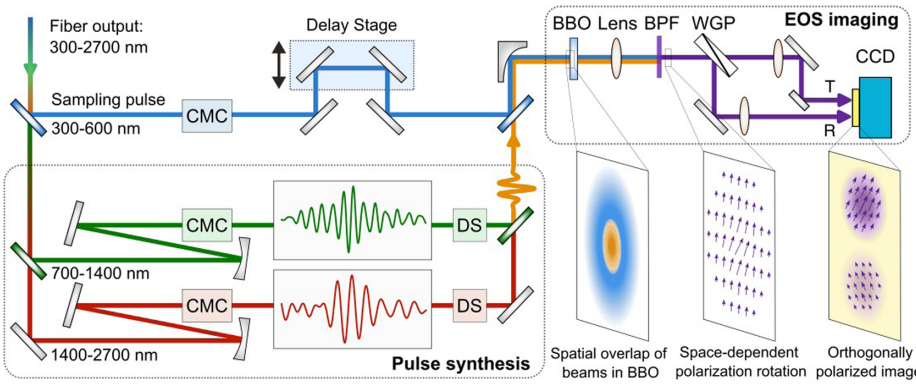

Fig. 1. Experimental setup. A supercontinuum spanning from 300 to 2700 nm is split into three channels for temporal compression using chirped mirror compressors (CMC). Two long-wavelengths channels (electric fields measured with EOS in the frames) are temporally superimposed with the delay stages (DS) for pulse synthesis, while the ultraviolet-visible channel is used as a sampling pulse in the EOS. All three channels after recombination are focused on a BBO, where the synthesized pulse is formed and mixed with the sampling pulse for sum frequency generation (SFG). A 4f imaging system images the BBO plane. The SFG emerging on the orthogonal axis shows a partial spectral overlap with the sampling pulse. A band-pass filter (BPF) is then used to isolate this spectral region. The "polarization rotation" effect of the sampling pulse in this filtered spectral range can be described and detected through interference of the sampling pulse and the SFG on the CCD. To trigger the interference, a wire-grid polarizer (WGP), oriented at 45° to the sampling pulse polarization, is placed. The reflected and transmitted through the WGP beams form two cross-polarized images, R and T, the subtraction of which yields the sampled electric field.

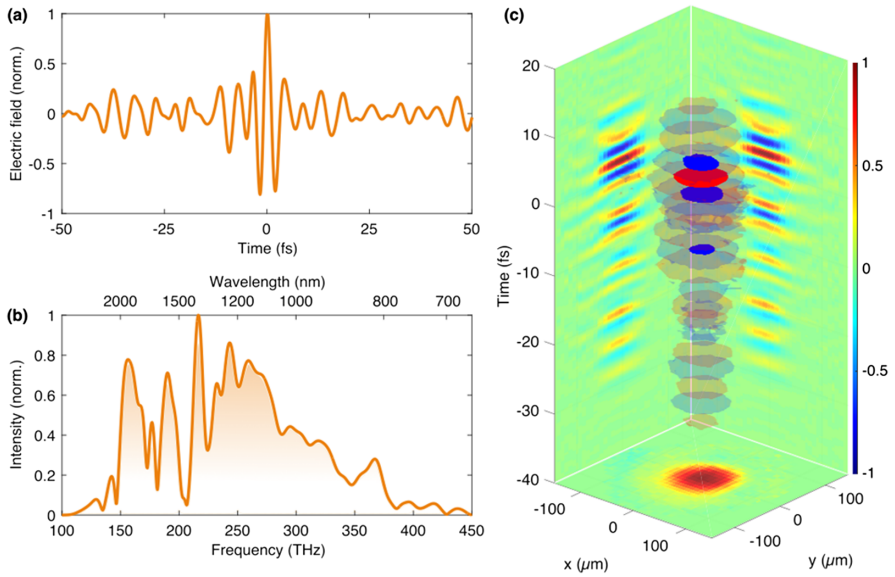

Fig. 2. (a) Electric field of a sub-cycle light transient $E(t)$ measured using standard electro-optic sampling (EOS). (b) Corresponding spectrum of the synthesized pulse obtained with the Fourier transform of the electric field in (a). (c) The extension of EOS to the imaging geometry allows the characterization of the generated pulse to include spatial coordinates $E(x, y, t)$. Semi-transparent and opaque contours in the 3D electric field image represent 12% and 60% of the maximum field value, respectively. The projections reflect the electric field at zero value of the corresponding coordinate, i.e., $E(0, y, t)$, $E(x, 0, t)$ and $E(x, y, 0)$.

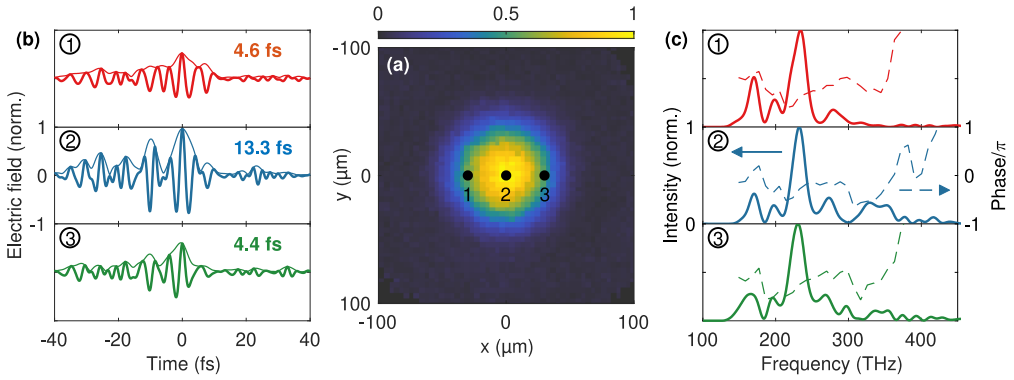

Fig. 3. Spatial analysis of the electric field structure. (a) Normalized intensity distribution of the synthesized pulse in the transverse x-y plane. (b) Temporal electric field of three pixels from (a) at (−30 μm, 0), (0,0), and (30 μm,0), with pulse durations of 4.6 fs, 13.3 fs, and 4.4 fs, respectively, measured as full-width at half-maximum of the squared envelope. (c) Corresponding spectrum and spectral phase obtained using the Fourier transform of the electric fields in (b).

4f imaging system with a NA of ∼ 0.064 and a magnification factor of ∼ 0.9 (Fig. 1). The band-pass filter (BPF) placed after the first lens isolates the spectral region, where the SFG and the LO overlap (290–360 nm). Importantly, the complete field information about the two-octave-spanning synthesized pulse is encoded into this relatively narrowband beam, which determines the spatial resolution and highly reduces chromatic aberrations of the imaging system. The interference of the orthogonally polarized SFG and the LO is triggered by a wire-grid polarizer (WGP), set at 45° relative to the sampling pulse polarization. Two beams, reflected R and transmitted T through the WGP, produce two images on the CCD. The subtraction and normalization of these images yield a field image E at each time delay,

$$E = \frac{R - T}{R + T}.$$

To enhance the image contrast, a thin-film polarizer centered at 343 nm was added after the BPF, balancing the intensities of the LO and the SFG on the CCD and increasing their interference depth [48]. For the analytical description of EOS imaging, simulations and the data acquisition and processing see Supplement 1 (S1). The spatiotemporal measurement of the synthesized pulse $E(x, y, t)$ is depicted in Fig. 2(c). Here, the projections are plotted at a zero value of the respective coordinates, i.e., $E(x, 0, t)$, $E(0, y, t)$, and $E(x, y, 0)$.

The recorded three-dimensional matrix of the electric field structure contains all spatiotemporal properties of the synthesized pulse. The integrated intensity distribution of the pulse in the x-y plane is shown in Fig. 3(a). To identify how the synthesized electric field varies across the space, we analyzed three individual pixels along the x-axis: at (−30 μm, 0), (0, 0), and (30 μm, 0). The temporal waveforms of these pixels presented in Fig. 3(b) illustrate spatial deviations of the field shape like the presence of a

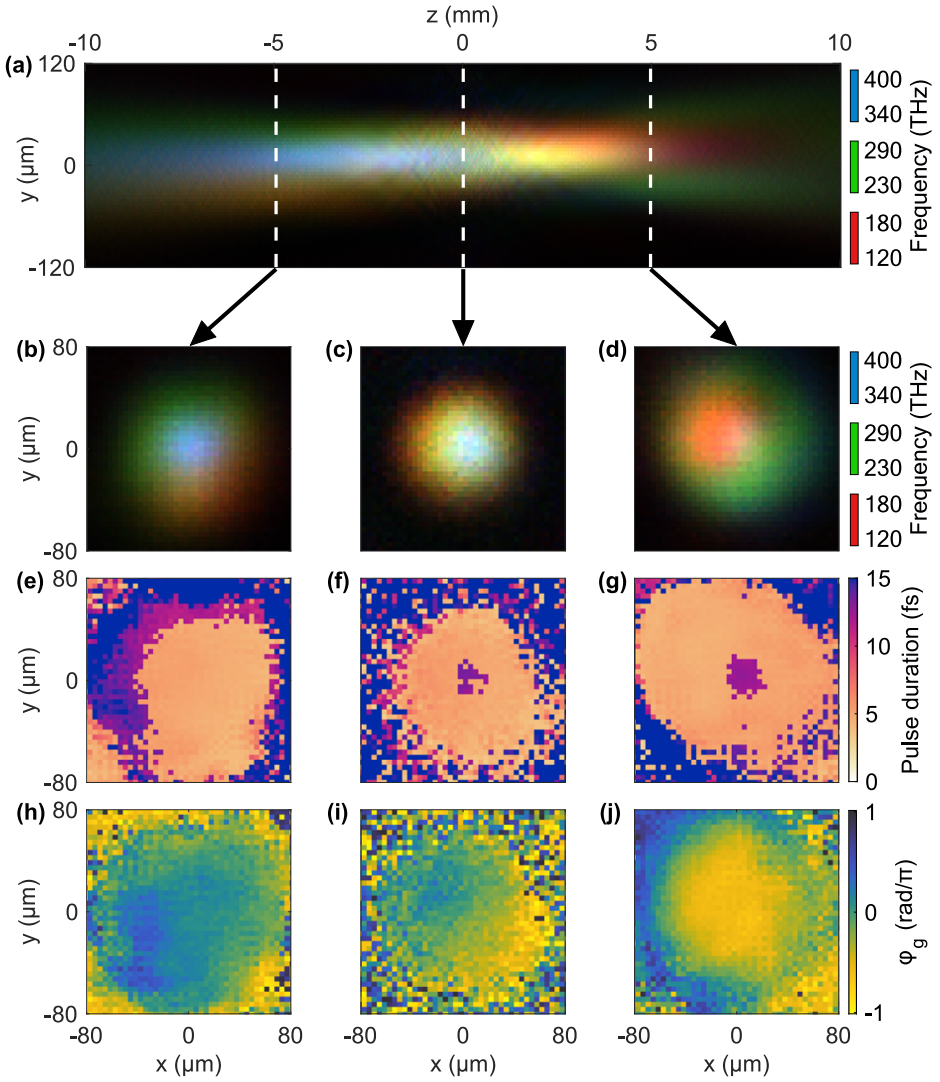

Fig. 4. Recorded electric field matrix is transformed to the hyperspectral image showing dynamics of the pulse around the focal point. (a) A false-color image demonstrating how the synthesized field was formed in the spatio-spectral domain along the z-axis. (b)–(d) Three slices of (a) at $z = -5$ mm, 0 mm (location of the actual measurement) and 5 mm. (e)–(g) Images presenting the distribution of pulse duration in the x-y plane at the positions corresponding to (b)–(d). (h)–(j) Images showing dynamics of the global phase φ_g in space.

strong satellite pulse at a time delay of −10 fs at the beam center. This satellite pulse increases the value of the pulse duration at the center (13.3 fs), while two outer pixels have nearly consistent values of 4.6 fs and 4.4 fs, respectively, calculated as full-width at half-maximum of the squared envelope. At the same time, the consistency in pulse durations does not reflect a uniformity of spectral characteristics. The spatio-spectral analysis shown in Fig. 3(c) exposes an interesting feature of this particular synthesized field: the high-frequency components are practically absent on the left side. The localization of low frequencies is greater in the pixel on the left, while the central pixel contains the full bandwidth reaching 450 THz.

To observe a complete picture of spatiotemporal dynamics of the field properties in the process of ultrabroadband pulse synthesis and to find the origin of the existing distortions, we demonstrate the superposition of the VIS-NIR and IR channels around the focal point. As a straightforward alternative to the physical displacement of the detection crystal, the field information along the z-axis, in the case of linear propagation, can be accessed with Fourier optics using the EOS measurement at a single z-plane [46]. Figure 4(a) presents a hyperspectral image of the superposition of the channels to show how the synthesized transient was shaped at the focus. To visualize the spectral distribution in a false-color image, the frequencies within the synthesized pulse are marked in the following way: the red color represents frequencies from 120 to 180 THz, the green denotes 230–290 THz, while the frequencies of 340–400 THz are indicated as blue. According to the image, the channels are superimposed with a small angle in the transverse direction, as the red-colored components are spatially displaced when crossing the focal point. In the longitudinal direction, the spectral components have an offset of ∼3 mm, mimicking strong chromatic aberrations. The same spatiotemporal analysis performed to the VIS-NIR and IR channels individually (see SI) shows that the chromatic aberrations are partially contained in the individual channel pulses, suggesting that the source of these distortions is the hollow-core fiber.

A detailed analysis of the spatio-temporal field structure at $z = -5$ mm, 0 mm (the actual location of BBO), and 5 mm has

been made to explore how the pulse duration and the global phase of the synthesized field vary in space as it crosses the focal point. Corresponding hyperspectral images in the x-y plane are shown in Figs. 4(b)–4(d). Calculating the pulse duration of the waveforms at each pixel [Figs. 4(e)–4(g)], one intriguing property of the propagating light transient becomes distinct: a local increase of the pulse duration emerges at the center of the beam as it passes the focal point and starts diverging. The extraction of the global phase φ_g at all the pixels presented in Figs. 4(h)–4(j) allows for the tracking of the global phase evolution over the spatial domain. As can be seen in the images representing the converging beam and the focus [Figs. 4(h) and 4(i)], the global phase gradually switches the value along the diagonals from $\pi/2$ to 0 and from 0 to $-\pi/2$, respectively. On the contrary, in the converging beam [Fig. 4(j)], the spatial transformation of the global phase follows a different, circular pattern changing its value from $-\pi$ at the beam center to over 0 at the marginal areas. It is worth noting that the spatial analysis of pulse durations and the global phase of the VIS-NIR and IR channels confirms that the observed effects are primarily the direct result of the superposition of the channels.

The ultrabroadband pulse synthesized with our laser setup has demonstrated a clear example of how the spatiotemporal distortions can be easily formed despite using the lowest number of spectral channels and a minimized set of optical elements in the design. In particular, sub-cycle transients with such global phase variations across space might lead to an unexpected, averaged response of the system when applied for field-sensitive experiments such as strong-field photoinjection [25] or high harmonic generation [49]. In this regard, the careful spatiotemporal sampling of the broadband electric fields can facilitate an accurate measurement of the physical properties of matter and better comparison with theoretical predictions.

4. CONCLUSION

In conclusion, we have presented field-resolved imaging of an ultra-broadband light transient produced using the synthesis of two octave-spanning channels in the visible and infrared spectral range. The recorded electric field information $E(x, y, t)$ has been used to reveal arbitrary spatio-temporal inhomogeneity formed during the pulse synthesis. Particularly, we showed how the electric field structure of the synthesized pulse varies across the x-y plane. Converting the recorded data to the spectral domain and numerically shifting the detection crystal along the z- direction, a complete picture of the superposition of the channels around the focal point has been retrieved, revealing the spatial dynamics of the pulse duration and the global phase along the propagation axis. The imaging technique is expected to enrich the metrology apparatus of attosecond physics regardless of the spatial complexity of the measured electric field structure, including beams carrying orbital angular momentum. EOS imaging will allow field-resolved detection to observe not only the space-averaged temporal dynamics of electrons and quasiparticles excited by sub-cycle light transients but also charge the migration in complicated systems such as photonic structures.

Funding. Max-Planck-Gesellschaft, Munich-Centre for Advanced Photonics; Air Force Office of Scientific Research (FA9550-16-1-0073); IMPRS-APS.

Disclosures. The authors declare no conflicts of interest.

Data availability. All data and image processing codes are available in the Edmond archive of the Max Planck Society, Ref. [50].

Supplemental document. See Supplement 1 for supporting content.

REFERENCES

1. P. Gaal, W. Kuehn, K. Reimann, *et al.*, "Internal motions of a quasiparticle governing its ultrafast nonlinear response," Nature **450**, 1210–1213 (2007).
2. M. Schultze, E. M. Bothschafter, A. Sommer, *et al.*, "Controlling dielectrics with the electric field of light," Nature **493**, 75–78 (2013).
3. M. Hohenleutner, F. Langer, O. Schubert, *et al.*, "Real-time observation of interfering crystal electrons in high-harmonic generation," Nature **523**, 572–575 (2015).
4. T. Higuchi, C. Heide, K. Ullmann, *et al.*, "Light-field-driven currents in graphene," Nature **550**, 224–228 (2017).
5. F. Schlaepfer, M. Lucchini, S. A. Sato, *et al.*, "Attosecond optical-field-enhanced carrier injection into the GaAs conduction band," Nat. Phys. **14**, 560–564 (2018).
6. M. Ossiander, K. Golyari, K. Scharl, *et al.*, "The speed limit of optoelectronics," Nat. Commun. **13**, 1620 (2022).
7. D. Zimin, N. Karpowicz, M. Qasim, *et al.*, "Dynamic optical response of solids following 1-fs-scale photoinjection," Nature **618**, 276–280 (2023).
8. A. Sommer, E. M. Bothschafter, S. A. Sato, *et al.*, "Attosecond nonlinear polarization and light–matter energy transfer in solids," Nature **534**, 86–90 (2016).
9. R. K. Shelton, L.-S. Ma, H. C. Kapteyn, *et al.*, "Phase-coherent optical pulse synthesis from separate femtosecond lasers," Science **293**, 1286–1289 (2001).
10. G. Krauss, S. Lohss, T. Hanke, *et al.*, "Synthesis of a single cycle of light with compact erbium-doped fibre technology," Nat. Photonics **4**, 33–36 (2010).
11. S.-W. Huang, G. Cirmi, J. Moses, *et al.*, "High-energy pulse synthesis with sub-cycle waveform control for strong-field physics," Nat. Photonics **5**, 475–479 (2011).
12. C. Manzoni, S.-W. Huang, G. Cirmi, *et al.*, "Coherent synthesis of ultrabroadband optical parametric amplifiers," Opt. Lett. **37**, 1880–1882 (2012).
13. G. M. Rossi, R. E. Mainz, Y. Yang, *et al.*, "Sub-cycle millijoule-level parametric waveform synthesizer for attosecond science," Nat. Photonics **14**, 629–635 (2020).
14. A. Alismail, H. Wang, G. Barbiero, *et al.*, "Multi-octave, CEP-stable source for high-energy field synthesis," Sci. Adv. **6**, eaax3408 (2020).
15. A. Wirth, M. Th. Hassan, I. Grguraš, *et al.*, "Synthesized light transients," Science **334**, 195–200 (2011).
16. M. Th. Hassan, T. T. Luu, A. Moulet, *et al.*, "Optical attosecond pulses and tracking the nonlinear response of bound electrons," Nature **530**, 66–70 (2016).
17. E. Ridente, M. Mamaikin, N. Altwaijry, *et al.*, "Electro-optic characterization of synthesized infrared-visible light fields," Nat. Commun. **13**, 1111 (2022).
18. E. Goulielmakis, M. Schultze, M. Hofstetter, *et al.*, "Single-cycle nonlinear optics," Science **320**, 1614–1617 (2008).
19. U. Morgner, R. Ell, G. Metzler, *et al.*, "Nonlinear optics with phase-controlled pulses in the sub-two-cycle regime," Phys. Rev. Lett. **86**, 5462–5465 (2001).
20. J. Itatani, F. Quéré, G. L. Yudin, *et al.*, "Attosecond streak camera," Phys. Rev. Lett. **88**, 173903 (2002).
21. K. T. Kim, C. Zhang, A. D. Shiner, *et al.*, "Petahertz optical oscilloscope," Nat. Photonics **7**, 958–962 (2013).
22. S. B. Park, K. Kim, W. Cho, *et al.*, "Direct sampling of a light wave in air," Optica **5**, 402–408 (2018).
23. M. R. Bionta, F. Ritzkowsky, M. Turchetti, *et al.*, "On-chip sampling of optical fields with attosecond resolution," Nat. Photonics **15**, 456–460 (2021).
24. Y. Liu, J. E. Beetar, J. Nesper, *et al.*, "Single-shot measurement of few-cycle optical waveforms on a chip," Nat. Photonics **16**, 109–112 (2022).
25. S. Sederberg, D. Zimin, S. Keiber, *et al.*, "Attosecond optoelectronic field measurement in solids," Nat. Commun. **11**, 430 (2020).
26. D. Zimin, M. Weidman, J. Schötz, *et al.*, "Petahertz-scale nonlinear photoconductive sampling in air," Optica **8**, 586–590 (2021).
27. N. Altwaijry, M. Qasim, M. Mamaikin, *et al.*, "Broadband photoconductive sampling in gallium phosphide," Adv. Opt. Mater. **11**, 2202994 (2023).

28. Q. Wu and X.-C. Zhang, "Free-space electro-optic sampling of terahertz beams," Appl. Phys. Lett. **67**, 3523–3525 (1995).
29. S. Keiber, S. Sederberg, A. Schwarz, *et al.*, "Electro-optic sampling of near-infrared waveforms," Nat. Photonics **10**, 159–162 (2016).
30. D. A. Zimin, V. S. Yakovlev, and N. Karpowicz, "Ultra-broadband all-optical sampling of optical waveforms," Sci. Adv. **8**, eade1029 (2022).
31. S. Akturk, X. Gu, P. Bowlan, *et al.*, "Spatio-temporal couplings in ultrashort laser pulses," J. Opt. **12**, 093001 (2010).
32. T. Amotchkina, M. K. Trubetskov, Y. Pervak, *et al.*, "Stress compensation with antireflection coatings for ultrafast laser applications: from theory to practice," Opt. Express **22**, 30387–30393 (2014).
33. A. Giree, M. Mero, G. Arisholm, *et al.*, "Numerical study of spatiotemporal distortions in noncollinear optical parametric chirped-pulse amplifiers," Opt. Express **25**, 3104–3121 (2017).
34. P. Gabolde and R. Trebino, "Single-shot measurement of the full spatio-temporal field of ultrashort pulses with multi-spectral digital holography," Opt. Express **14**, 11460–11467 (2006).
35. P. Bowlan, P. Gabolde, A. Shreenath, *et al.*, "Crossed-beam spectral interferometry: a simple, high-spectral-resolution method for completely characterizing complex ultrashort pulses in real time," Opt. Express **14**, 11892–11900 (2006).
36. B. Alonso, Í. J. Sola, Ó. Varela, *et al.*, "Spatiotemporal amplitude-and-phase reconstruction by Fourier-transform of interference spectra of high complex-beams," J. Opt. Soc. Am. B **27**, 933–940 (2010).
37. S. L. Cousin, J. M. Bueno, N. Forget, *et al.*, "Three-dimensional spatiotemporal pulse characterization with an acousto-optic pulse shaper and a Hartmann–Shack wavefront sensor," Opt. Lett. **37**, 3291–3293 (2012).
38. M. Miranda, M. Kotur, P. Rudawski, *et al.*, "Spatiotemporal characterization of ultrashort laser pulses using spatially resolved Fourier transform spectrometry," Opt. Lett. **39**, 5142–5145 (2014).
39. A. Borot and F. Quéré, "Spatio-spectral metrology at focus of ultrashort lasers: a phase-retrieval approach," Opt. Express **26**, 26444–26461 (2018).
40. N. C. J. van der Valk and P. C. M. Planken, "Electro-optic detection of subwavelength terahertz spot sizes in the near field of a metal tip," Appl. Phys. Lett. **81**, 1558–1560 (2002).
41. J. Blöchl, J. Schötz, A. Maliakkal, *et al.*, "Spatiotemporal sampling of near-petahertz vortex fields," Optica **9**, 755–761 (2022).
42. V. Hanus, B. Fehér, V. Csajbók, *et al.*, "Carrier-envelope phase on-chip scanner and control of laser beams," Nat. Commun. **14**, 5068 (2023).
43. Q. Wu, T. D. Hewitt, and X.-C. Zhang, "Two-dimensional electro-optic imaging of THz beams," Appl. Phys. Lett. **69**, 1026–1028 (1996).
44. F. Blanchard, A. Doi, T. Tanaka, *et al.*, "Real-time terahertz near-field microscope," Opt. Express **19**, 8277–8284 (2011).
45. F. Blanchard, J. E. Nkeck, L. Guiramand, *et al.*, "Two-dimensional space–time terahertz memory in bulk $SrTiO_3$," Optica **9**, 980–986 (2022).
46. M. Mamaikin, Y.-L. Li, E. Ridente, *et al.*, "Electric-field-resolved near-infrared microscopy," Optica **9**, 616–622 (2022).
47. E. Ridente, M. Weidman, M. Mamaikin, *et al.*, "Hybrid phase-matching for optical parametric amplification of few-cycle infrared pulses," Optica **7**, 1093–1096 (2020).
48. M. Mamaikin, E. Ridente, N. Altwaijry, *et al.*, "Contrast enhancement in near-infrared electro-optic imaging," Opt. Express **30**, 18179–18188 (2022).
49. N. Ishii, K. Kaneshima, K. Kitano, *et al.*, "Carrier-envelope phase-dependent high harmonic generation in the water window using few-cycle infrared pulses," Nat. Commun. **5**, 3331 (2014).
50. https://edmond.mpg.de/.